Green synthesis of functionalized graphene-based material with dimethyl but-2-ynedioate for electrochemical energy storage devices

Journal of Energy Storage 90 (2024) 111857

Contents lists available at ScienceDirect

Journal of Energy Storage

journal homepage: www.elsevier.com/locate/est

Research papers

Green synthesis of functionalized graphene-based material with dimethyl but-2-ynedioate for electrochemical energy storage devices

Silvia Mazzotta [a,b,d,*], Alberto Martis [a,c], Mara Serrapede [a,c], Pietro Zaccagnini [a,c], Francesca Risplendi [c], Stefano Bianco [c], Giancarlo Cicero [c], Francesca Verga [a,b], Fabrizio Pirri [a,c], Andrea Lamberti [a,c], Sergio Bocchini [a,c,**]

[a] Center for Sustainable Future Technologies Istituto Italiano di Tecnologia, Via Livorno 60, Torino 10144, Italy
[b] Dipartimento di Ingegneria dell'Ambiente, del Territorio e delle Infrastrutture (DIATI) Politecnico di Torino, Corso Duca degli Abruzzi 24, Torino 10129, Italy
[c] Dipartimento di Scienza Applicata e Tecnologia (DISAT), Politecnico di Torino, Corso Duca degli Abruzzi 24, Torino 10129, Italy
[d] University School for Advanced Studies IUSS Pavia, Palazzo del Broletto-Piazza della Vittoria 15, Pavia 27100, Italy

ARTICLE INFO

Keywords:
Graphene
Diels-Alder
Microwave assisted synthesis
DFT
Li-ion electrodes

ABSTRACT

Functionalization of graphene with dimethyl acetylenedicarboxylate is achieved through a microwave-assisted Diels-Alder reaction. The physical, chemical, and electrochemical properties of the modified sheets are thoroughly investigated by complementary characterization techniques. Density Functional Theory calculations are employed to examine the functionalization mechanism and to highlight the role of defects such as epoxide bridges introduced in graphene during exfoliation. Our findings provide valuable insights into the development of efficient and cost-effective methods for large-scale production of high-quality graphene-based materials. Specifically, the electrochemical properties of anode materials containing functionalized graphene are evaluated for Li-ion electrochemical energy storage devices, demonstrating excellent electrochemical reversibility and rate capability. The cyclic voltammetry analysis reveals material stabilization after a few cycles, resulting in a coulombic efficiency of up to 95 % and a discharge capacity of 162.3 $mA{\cdot}h{\cdot}g^{-1}$. The galvanostatic cycling test indicates that the material electrode retains 57 % of its initial capacity at a C-rate of 10C, indicating high-power capability. These promising results position organic modified graphene as a potential material for Li-ion capacitors, with a specific capacity that aligns with the last intercalation stage capacity at a lower potential. Overall, the study's findings offer significant contributions to the advancement of graphene-based materials in energy storage applications.

1. Introduction

Graphene, a material with a wide range of chemical, environmental, industrial, and electronic applications, has garnered significant interest from researchers worldwide. Various methods, including mechanical cleavage, liquid-phase exfoliation (LPE), gas-phase synthesis, chemical vapor deposition (CVD), and electrochemical reaction were used to produce graphene. These methods have been widely studied and reported in scientific literature [1–4].

Among the various synthetic methods for graphene, liquid-phase exfoliation (LPE) using natural graphite has gained particular attention due to its low cost and potential for large-scale production. Sonication-assisted LPE has emerged as a powerful tool for the chemical preparation of single- and few-layer graphene [5]. Ultrasound has been shown to have unique and powerful effects in the fabrication of graphene, and the sonication conditions (such as mild bath sonication) can be modified to produce different graphene materials, including low-defect or defect-free materials. This versatility makes sonication-assisted LPE an attractive method to produce high-quality graphene [6,7].

Diels-Alder (DA) is an interesting reaction for the covalent functionalization of graphene since it is a one-step reaction which does not require any catalyst and typically occurs in mild reaction conditions. In 2012, [8] Sharkar et al. first reported DA reaction using graphene as the

* Correspondence to: S. Mazzotta, Dipartimento di Ingegneria dell'Ambiente, del Territorio e delle Infrastrutture (DIATI) Politecnico di Torino, Corso Duca degli Abruzzi 24, Torino 10129, Italy.
** Correspondence to: S. Bocchini, Dipartimento di Scienza Applicata e Tecnologia (DISAT), Politecnico di Torino, Corso Duca degli Abruzzi 24, Torino 10129, Italy.
E-mail addresses: silvia.mazzotta@polito.it (S. Mazzotta), Sergio.Bocchini@polito.it (S. Bocchini).

https://doi.org/10.1016/j.est.2024.111857
Received 12 December 2023; Received in revised form 28 March 2024; Accepted 22 April 2024
Available online 2 May 2024

diene and maleic anhydride (MA) as dienophile occurring at a temperature of about 120 °C [9]. Zhang et al., in 2020, carried out one-step functionalization of graphene via DA reaction by a catalyst-free approach at 90 °C for 12 h using dimethylformamide (DMF) as the solvent [10].

Ethylene tetracyanate has been shown to have good reactivity with graphene due to the presence of cyano electron-attractor groups, which give the molecule a high dienophilicity [11] This allows for cycloaddition with graphene to occur at room temperature in the presence of dioxane and dichloromethane.

In 2019, Feng et al. [12] developed a method for exfoliating graphite into graphene nanosheets in situ, within a rubber and graphite blend, using the Diels–Alder reaction under strong shear force but only reducing the thickness of the exfoliated graphite to a range of 0.1–1 μm.

In 2021 Zhang et al. [13] propose a route for exfoliating graphene based on the Diels-Alder reaction. In their method, N-(4-hydroxyl phenyl) maleimide is used as reactive intercalating agent to increase the interlayer spacing of graphite. Graphene is thus prepared by exfoliation of graphite using ultrasound. Finally in 2022 Tokamav et al. use furfuryl amine to produce few layers graphene via mechanochemical process by a Diels Alder cycloaddition and generate pure few layer graphene by reversing the reaction by thermal treatment [14].

Graphite is highlighted as a well-established material in Li-ion intercalation energy storage devices such as batteries [15] and supercapacitors [16]. By moving from amorphous to oriented phases (crystalline), carbon changes its storage mechanism with respect to Li-ion accumulation [17]. Nowadays, energy storage devices are moving to high-power and high-energy density systems, hence, the development of materials able to fulfil these requirements is of strong interest. Modification of natural graphite flakes has reported with the aim to increase specific capacity and cycle life [18].

Li-ion capacitors, also known as lithium-ion capacitors or LICs, are introduced as a promising energy storage technology that combines the high energy density of lithium-ion batteries with the high-power capability of supercapacitors. They act as a hybrid energy storage system, bridging the gap between traditional capacitors and batteries, and offering a balance between energy and power performance.

Recent advancements in Li-ion capacitors have been driven by ongoing research and development efforts, aiming to enhance energy storage capacity, power density, cycling stability, and overall performance. One area of improvement in Li-ion capacitors focuses on the development of advanced electrode materials. Researchers are investigating carbon-based materials such as activated carbon, graphene, and carbon nanotubes to increase energy storage capacity and improve charge-discharge efficiency [19–22].

In this investigation, our objective was to unravel the intricacies of graphene's covalent functionalization via a synergistic approach that melds computational analyses with experimental practices. Central to our study was the exploration of graphene's reactivity in the Diels-Alder (DA) reaction, observed across a temperature spectrum from 25 °C to 175 °C. This examination was facilitated by the employment of a microwave reactor, chosen for its adeptness in ensuring precise temperature regulation and homogeneity [23]. The integration of microwave technology in organic synthesis marries innovation and efficiency, creating an unparalleled platform for probing chemical reactions beyond the capabilities of conventional heating methodologies [24–27]. This methodological fusion allows for expedited, even heating holding the promise of leading to the uncovering of novel compounds and fostering the development of more sustainable, environmentally friendly chemical processes [28,29].

We studied the reactivity of graphene with dimethyl acetylenedicarboxylate (DMAD). A mechanistic study based on density functional theory (DFT) was employed to comprehend the functionalization mechanism and to elucidate the role of stabilization brought about by the defects introduced during the exfoliation process. Then, the chemical and physical properties of the resulting products were characterized, as well as their electrochemical properties.

2. Experimental section

2.1. Materials

NMP (1-Methyl-2-pyrrolidone, 95 %), chloroform (≥99,8 %), dimethyl acetylenedicarboxylate (95 %), dioxane (≥99 %), graphite flakes (99 % carbon basis,- 325 mesh particle size), methanol (≥99,8 %), MHQ (Methyl hydroquinone, 99 %), toluene (99,8 %) were purchased from Sigma-Aldrich. A solution of 1 M $LiPF_6$ (LP30) in 1:1 vol. of EC: DMC (ethylene carbonate: dimethyl carbonate), battery grade, was purchased from Solvionic.

2.2. Synthesis procedure for graphene with dimethyl-acetylenedicarboxylate

Graphene was synthesized utilizing a modified version of the Coleman method as described in ESI S1.1 [30,31], and detailed in our manuscript [32]. Initially, 1 g of graphite powder flakes was exfoliated in 50 ml of *N*-methyl-2-pyrrolidone (NMP) under well-controlled temperature conditions, specifically maintained below 10 °C to prevent any thermal degradation of the material or solvent. This suspension was subjected to bath sonication for a duration of 80 min, employing a frequency of 37 kHz and a power output of 320 W. The use of an ice bath was crucial to maintain the low-temperature condition throughout the sonication process, ensuring efficient exfoliation while minimizing the risk of overheating.

Following sonication, the mixture was centrifuged at 4200 rpm for 45 min. The supernatant, containing exfoliated graphene, was carefully decanted and stored for further use. This process results in a graphene dispersion presumed to have a concentration of approximately 80 μg mlˆ-1. 150 ml of the graphene dispersion was sonicated at room temperature for 10 min and filtered using a hydrophilic nylon membrane (Milipore 0.20 μm, 47 mm) under vacuum. The filtered dispersion was then sonicated again at room temperature for 15 min in a 10 ml glass microwave reactor, using either toluene or a 50 % wt chloroform/dioxane solution as the solvent. Dimethyl acetylenedicarboxylate (0.5 ml) was added to the resulting dispersion under a nitrogen flow, and the reaction was carried out in a closed silicon carbide reactor under stirring for 1 h, using an Anton Paar Monowave 200 microwave reactor.

The resulting product was filtered under vacuum using an alumina filter (Milipore 0.2 μm, 47 mm), washed, and dried in a vacuum oven for 12 h at 60 °C, resulting in the production of graphene films (see Fig. 1). All samples were synthesized using this method, except for the M175mhq sample, which was prepared by adding 18 mg of methyl

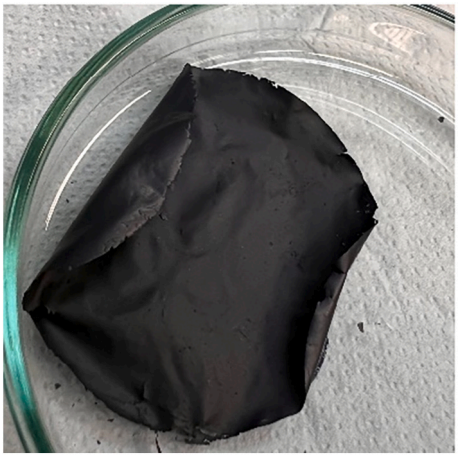

Fig. 1. Functionalized Graphene based material (M60).

hydroquinone. Table 1 provides a description of the conditions used for each of the samples.

2.3. Electrodes preparation procedure for electrochemical analyses

The potential use of the M60 sample as an electrode material in energy storage devices was evaluated. To prepare the electrode, a viscous slurry was formed by mixing M60 with Polyvinylidene Fluoride (PVDF) in N-Methyl-2-pyrrolidone (NMP) at a weight ratio of 9:1. The slurry was deposited onto a copper current collector using a doctor blade procedure at a speed of 10 mm s^{-1}, resulting in electrodes with a diameter of 12 mm. The electrodes were then vacuum-dried overnight at 40 °C to remove any remaining solvent traces. The vacuum pump used did not have a pressure gauge, but the expected vacuum level was below 10^{-4} bar.

To minimize oxygen and moisture contamination, the cell assembly was carried out in an MBraun glove box system filled with nitrogen gas, with the levels of oxygen and moisture kept below 0.5 ppm. The resulting mass loading of the electrode was 0.88 mg cm^{-2}.

2.4. Characterizations

Raman Spectroscopy. Raman spectra were acquired using a Renishaw inVia Reflex micro-Raman spectrophotometer (Renishaw plc, Wotton-under-Edge, UK) equipped with a cooled CCD camera. The samples were excited with a diode laser source operating at a wavelength of 514.5 nm and approximately 5 mW power. A 50× objective was used for sample inspections under backscattered light collection conditions [33].

Thermogravimetric analysis coupled with vapor phase infrared spectroscopy (TGA-IR). TGA-IR was used to characterize all samples. The measurements were performed using a NETZSCH TG209 F1 Libra thermogravimetric analyser (TGA) coupled to a Bruker Tensor II Fourier transform spectrophotometer equipped with a DTGS detector. Approximately 10 mg of each sample was placed in an alumina crucible and heated under a nitrogen flow (40 ml min^{-1}) from 30 to 800 °C at a rate of 10 °C min^{-1}. Infrared spectra were continuously acquired in the absorbance mode over the range of 4000 to 600 cm^{-1} with a resolution of 2 cm^{-1} during the heating process [34].

X-ray Diffraction Analysis (XRD). X-ray diffraction (XRD) analysis was conducted using a PANalytical X'Pert MRD Pro powder diffractometer equipped with a 1D PIXcel detector (Malvern PANalytical, United Kingdom). Diffractograms were collected in Bragg-Brentano reflection mode using Cu Kα radiation, at an operating voltage of 40 kV and a tube current of 40 mA. The instrumental broadening was calculated using the Caglioti equation based on the reflections of a standard LaB_6 powder (NIST660a). Measurements were carried out in continuous mode with a step size of $2\theta = 0.0131°$ and a data time per step of 150 s for the natural graphite sample and 300 s for the membrane sample. QualX software, with the COD database, was used for qualitative phase determination, and MAUD software was used for quantitative analysis and refinement. The COD cards matching the diffraction patterns of the graphite are 00–900-8569 (space group P63mc) and 00–901-2705 (space group R-3 m) [35].

UV–Vis Spectroscopy (UV–vis). Absorption spectra were recorded using a Perkin-Elmer LAMBDA 650 S UV/Vis/NIR spectrometer in the absorption mode. To prepare the samples, each was dispersed in ethanol and the blank solvent spectrum was subtracted from the recorded spectrum [36].

Fluorescence Spectroscopy. Fluorescence spectra were performed in a PerkinElmer precisely LS55 Fluorescence Spectrometer equipped with Low Temp Lumin Accessory. Sample was dispersed in Ethanol and the selected excitation wavelength was at 266 nm [37,38].

Electrochemical characterization. The electrochemical analyses were conducted in a half-cell configuration in a Swagelok Tee cell. The working electrode (WE) was prepared by depositing the M60 sample onto a copper current collector. Metallic lithium was used as both the counter electrode (CE) and the reference electrode (REF), and the Whatman fiberglass of grade D (GFD) served as separator. The LP30 electrolyte solution was used, and the electrolyte amount was 200 µl. Electrochemical measurements were performed using a VMP 3 potentiostat provided by BioLogic. The instrument offered a voltage range of ±10 V, a maximum current of 400 mA, with a voltage and current resolution of 50 µV (minimum) and 760 pA, respectively. The accuracy was declared to be <0.1 % of the full-scale range. The electrometer had an input impedance >1 TΩ, a capacitance of <20 pF, and an offset current lower than 5 pA.

Cyclic voltammetry (CV). analyses were performed at 0.2 mV s-1 in the potential window [0.1, 1.5] V vs. Li/Li + to investigate the electrode thermodynamics, as suggested by La Mantia et al. [39]. The voltage resolution was 100 µV, and the current was recorded by sampling 100 % of the voltage step, averaged over 10 points. The resulting sampling conditions were 1 point per mV voltage variation. Further CV analyses were performed in the potential window [0.0, 1.5] V vs. Li/Li+. Galvanostatic charge and discharge (GCD) measurements were performed at different C-rates, set by referring to graphite's theoretical specific capacity of 372 mAh g^{-1}. The different C-rates were {1/10, 1/5, 1/2, 1, 2, 5, 10} C.

Electrochemical Impedance Spectroscopy (EIS). was performed to study the frequency response of the synthesized electrodes. The probe signal was 5 mV peak amplitude, and the frequencies varied from 1 MHz to 10 mHz, with 10 points per decade. Each frequency point was averaged over at least three periods.

2.5. Computational details

Theoretical calculations are performed using density functional theory (DFT) and time-dependent density functional theory (TDDFT), as implemented in the Quantum Espresso simulation package [40,41] The electron wave functions are expanded in plane waves (PWs), while exchange and correlation effects are modelled by the generalized gradient approximation (GGA) for the exchange-correlation functional proposed by Perdew, Burke and Ernzerhof (PBE) [42]. The electron-ion interaction is described by optimized ultrasoft pseudopotentials [43]. Kohn-Sham states (electron density) were expanded into plane waves with a kinetic energy cutoff of 30 Ry (300 Ry). To include long-range dispersion corrections to standard Kohn-Sham DFT, the Grimme-D3 method was utilized [44]. The Brillouin zone of graphene unit cell was sampled with a 12 × 12 × 1 shifted Monkhorst-Pack mesh [45] and reduced accordingly for supercell calculations while the Brillouin zone of molecular cluster was sampled at the Γ point. A vacuum region of at least 10 Å was added in the non-periodic directions to prevent spurious interactions between the periodic replicas. All structures were relaxed by minimizing atomic forces, and convergence was achieved when the maximum component of residual forces on ions was $<10^{-5}$ Ry/bohr.

To understand how likely a reaction is to occur between the graphene sheet and a given organic molecule we calculated the functionalization reaction energy as follows:

Table 1
Sample of functionalised graphene.

Samples	Temperature	Solvent
Name	(°C)	Type
Mrt	25	Toluene
Mrt_cd	25	Chloroform: Dioxane[a]
M60	60	Toluene
M125	125	Toluene
M135	135	Toluene
M175	175	Toluene
M175mhq[b]	175	Toluene

[a] 1:1 by weight.
[b] MHQ added.

$$\Delta E = E_{tot} - (E_{mono} + E_{mol})$$

where E_{tot} represents the total energy for the functionalized structure while E_{mono} and E_{mol} correspond to the total energy of the relaxed graphene monolayer (either pristine or with specific single point defects) and that of the isolated molecule, respectively. We utilized the climbing image nudged elastic band method (CI-NEB) to identify the activation barriers of the chemical reactions involved in the functionalization process [46].

Optical spectra were simulated using the Liouville-Lanczos approach to linearized TDDFT, as implemented in the turboTDDFT code [47]. In this case, the Heyd-Scuseria-Ernzerhof (HSE) hybrid functional was utilized [48,49] and 3000 iterations were calculated to obtain accurate optical spectra.

3. Results and discussion

To assess the functionalization of the material, a range of analytical techniques were employed, including TGA-IR, UV–Vis, Emission, and Raman analyses.

3.1. UV–Vis analysis

The UV–Vis spectroscopic analysis of the graphene and the other functionalized materials revealed the presence of two distinct absorption bands (Table 2, ESI Fig. S4). The first band, which appeared at 265 nm, can be attributed to the characteristic π → π* transition associated with the –C=C- bonds present in the graphene's aromatic rings. The second intense band, observed at 203 nm, is correlated with the n → π* transition of the C—O groups presents in the ester functional groups of the material. Typically, this band is observed within the range of 200–210 nm and may be due to the oxide defects formed during the microwave reaction. Notably, M60 and Mrt_cd exhibited different spectra, with a single absorption maximum at 267 nm and 266 nm, respectively.

The spectra of Mrt, M125 M135, M175 and M175mhq showed remarkably similar peaks thus only a comparison between Mrt and M125 is reported in Fig. 2a, with Mrt exhibiting peaks at 203 and 253 nm, while M125 had peaks at 203 and 254 nm. In contrast, M60 and Mrt_cd showed a single peak with a broad band at 266 and 267 nm, respectively, indicating variations in the graphene's absorption bands, in Fig. 2b M60 is reported.

The observed variations in the absorption bands of M60 and Mrt_cd suggest that they have undergone chemical functionalization, which is often indicative of the presence of new chemical groups or bonding interactions with other molecules. To confirm this, a fluorescence spectrum was performed on Mrt_cd, which is a common technique used to study the chemical and physical properties of materials. The fluorescence test provided further insights into the nature of the functionalization, confirming the presence of chemical modifications in the graphene samples.

3.2. Fluorescence analysis

Fluorescence spectra was obtained in the modes of synchronous-scan excitation on dispersed sample in ethanol. The emission spectrum is recorded by measuring the relative intensity of radiation emitted as a function of the wavelength at a constant excitation wavelength (λ_{ex}) at 266 nm. Fig. 3 exhibits the fluorescence emission spectra which reports two strong emission peaks (λ_{em}) at 527 and 538 nm. The presence of emission peaks may be correlated with the structural disorder induced by the introduction of DMAD into the material [37,38].

Table 2
UV–Vis Absorbance wavelength (λ) of functionalized graphene compound in alcoholic solution.

Mrt (nm)	Mrt_cd (nm)	M60 (nm)	M125 (nm)	M135 (nm)	M175 (nm)	M175mhq (nm)
203	-	-	202	208	206	208
253	266	267	254	253	265	254

3.3. Raman spectroscopy

Raman spectroscopy was performed on all samples, and the results are presented in Fig. 4 and Table 3. The pristine material exhibited the typical features of exfoliated graphene material, with three main peaks observed in the spectrum: the D band at 1352 cm^{-1}, the G band at 1582 cm^{-1} (in-plane vibration of sp2 carbon atoms), and the 2D band at 2712 $cm^{-}1$ [32,33]. The D band is related to the defectiveness in the sp^2 domains, as it is due to the A1g breathing vibrations of six-membered sp^2 carbon rings, becoming Raman-active when the symmetry of the nearby lattice is reduced by defects or functional groups in the material. The G band originates from a first-order inelastic scattering process involving the degenerate iTO and iLO phonons at the G point (E2g mode). Close to the G band, a weaker D′ peak at 1620 cm^{-1} can be observed, again related to the amount of disorder in the lattice. The 2D band is the second order of the D band, involving two iTO phonons near the K point.

In contrast to the D band, the 2D band is allowed without any kind of disorder or defects, and its shape depends on the number of graphene layers, with multiple peaks convolution [33,50] The intensity ratio between the D peak and G peak is related to the mean dimension LD of the graphenic domains, as I_D/I_G is proportional to LD-alpha, where alpha = 1 for edge defects [51] and alpha = 2 for point defects. Thus, the increase of the I_D/I_G ratio reflects the augmented defectiveness of the graphenic materials. From the data reported in Table 3, it is possible to observe an increase in the I_D/I_G ratios for all the treatments performed, except for the mild room temperature treatment in toluene where the augment is negligeable. The maximum effect ($I_D/I_G = 0.79$) is observed when 50 % chloroform and 50 % dioxane are chosen as the solvent solution, sample Mrt_cd and M60, but the effect is remarkable for all the treatments proposed. Furthermore, a downshift in the 2D peak position and a more symmetric profile are evidenced after all the functionalization treatments.

3.4. TGA analysis

As reported in our previous work by Martis et al. [32], the TGA thermogram of graphite has a continuous loss trend and shows a weight residue value of 96,9 % at 799 °C. The graphene (Mrt) TGA analysis has one single weight loss step, around 700 °C of about 50%wt. The difference in the mass change trends of graphite and exfoliated graphene is a direct consequence of the top-down strategies used in the exfoliation process, which induce some defects into graphene sheets and increase the oxidation degree. This effect has been reported in multiple studies, including Dato et al. [3] and by Xu et al. [6].

Thermal stability of the compounds was examined using TGA-IR analysis, which revealed a two-step degradation process (refer to SI for details). The first degradation occurred at around 300 °C, followed by a second degradation at around 650 °C. The residual mass at 800 °C was approximately 45 % for all compounds, except for M125 and M175, which had a residual mass of around 65 %. Gas-phase IR analysis at different temperatures showed the presence of water (two broad bands at 4000–3500 and 1800–1300 cm^{-1}), CO_2 (four peaks around 3500 cm^{-1} and a double peak at 2350 cm^{-1}), and carbon monoxide (two bands at 2150 cm^{-1}) for all compounds. However, the IR spectra of Mrt_cd and M60 (Fig. 5) at different temperatures did not show any water bands meaning a less hydrophilic structure and/or the loss of oxygen present in the structure. In particular, the M60 spectra showed peaks at 1738 cm^{-1}, which can be attributed to the C═O stretching of the COOEt group, confirming the functionalization.

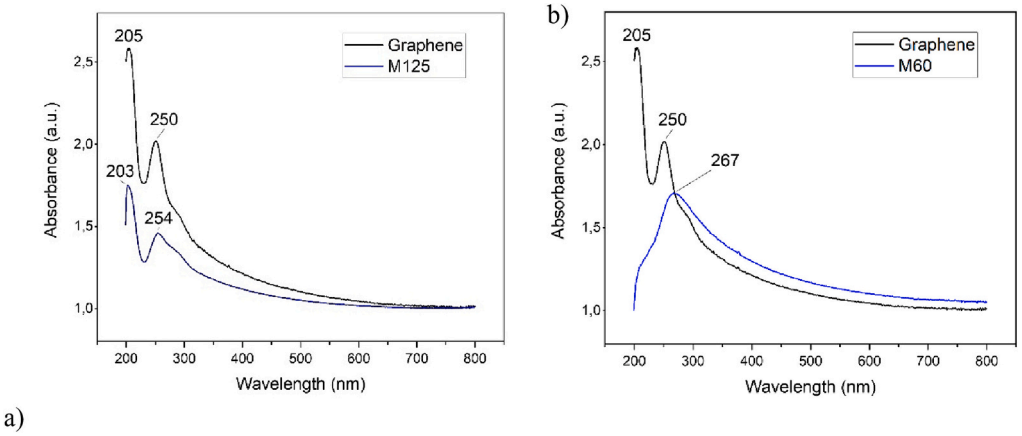

Fig. 2. Comparison between UV–Vis Spectra of a) Graphene and M125, and b) Graphene and M60.

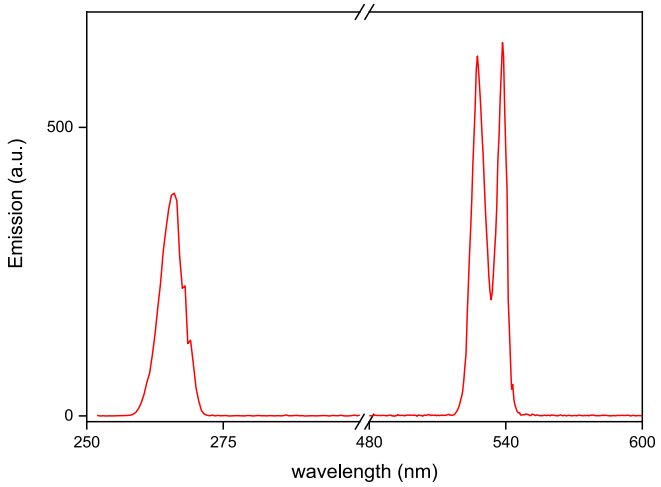

Fig. 3. Fluorescence Emission Spectra of M60.

To provide context for comparison, it is worth noting that pure dimethyl acetylenedicarboxylate has a flash point of 86 °C (closed cup) and a boiling point of 95–98 °C at 25 hPa. The TGA-IR analysis of M60 revealed no weight loss at or near 100 °C that could be attributed to the evaporation of free alkyl groups. The initial part of the thermogram of M60 followed the trend of unfunctionalized graphene up to 200 °C. However, a weight loss of 7 % was observed after this point, with a maximum degradation velocity at 377 °C, which could be associated with the presence of tailored dimethyl acetylenedicarboxylate.

3.5. X-ray diffraction analysis

To determine whether functionalization could significantly affect the engineering of the material to produce self-standing membranes for energy-related applications (self-standing ion-selective membranes or electrodes for flow-electrochemical cells i.e. fuel cells, redox-flow batteries, capacitive deionization, ….), the diffraction pattern together with the electrochemical activity of the M60 was compared to that of the pristine material.

The diffraction pattern of the pristine material shows a multiplicity of broad and sharp peaks. The major broad peak is centred at 11 degrees (2q) and it is often linked to graphene oxides [35]. This feature has been highlighted in the *Pristine* pattern presented in Fig. S29 in the Supporting Information, while in the main article, the broad peak has been included in the background correction of the pattern only to appreciate the crystalline peaks. The sharp peaks reveal the presence of two symmetries

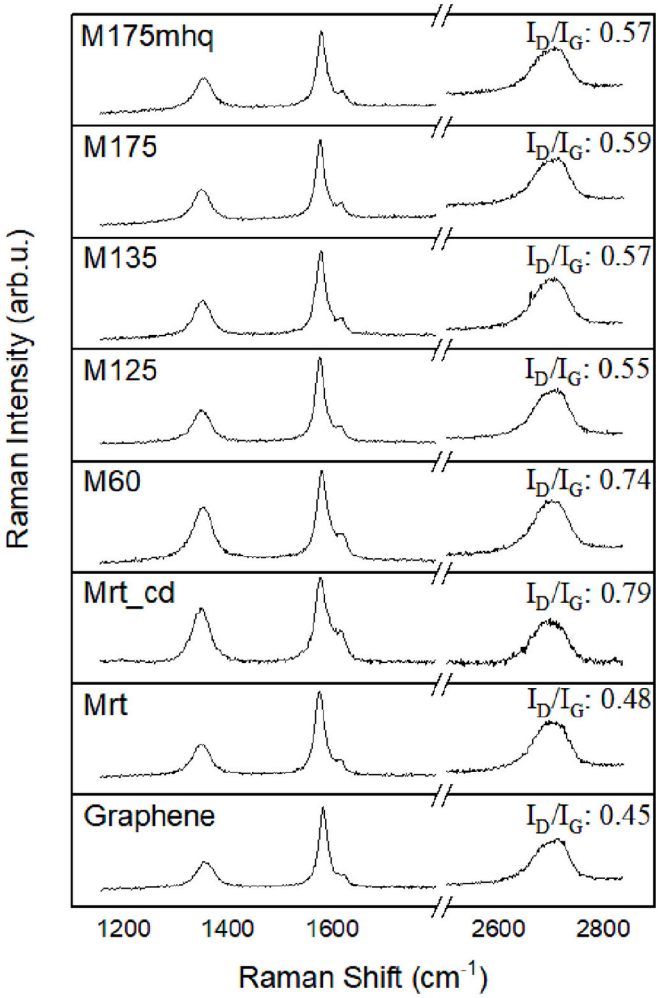

Fig. 4. Raman spectra of Graphene before and after functionalization.

of the graphite which are the P63mc (COD code 00–900-8569) which is the 77,18 % of the crystalline part of the powder and the R-3:R (COD code 00–901-2705) which is the remaining 22,82 %. Those two phases are evidenced in Fig. 6a and b from the blue and red pattern, respectively. From the Reitveld refinement, the crystallite size of the two phases are, according to the turbostratic model [52], of about 470 and 395 Å with similar microstrain of 1.4u and 1.7u, respectively. The sample M60 instead, presents the P63mc phase alone, without any

Table 3
Raman spectra Position of D, G peaks of graphene before and after functionalization and intensity ratio I_D/I_G values.

Sample	Peak positions cm^{-1}		
	D	G	2D
M175mhq	1350	1579	2705
M175	1348	1577	2707
M135	1354	1579	2705
M125	1350	1575	2707
M60	1354	1579	2690
Mrt_cd	1350	1577	2698
Mrt	1352	1575	2696
Graphene	1352	1582	2712

broadening associated to GO or short-range order of phases. The cell parameter *c* related to the distance between the graphene layers of the graphite shortened with respect to that of the pristine powder, decreasing from 6.7258 Å to 66,821 Å in the self-standing sample, indicating a densification of the material. The average crystalline size also decreased to 173 Åwell evidenced from the enlargement of the FWHM of the (002) peak shown in Fig. 6c. Moreover, it is worth noticing that M60 presents strong preferential orientation along the (00*l*) crystalline directions, consistent with the membrane formation procedure. The basic parameters retrieved form the refinement is reported in the Supporting Information in Table S2.

3.6. DFT model

TGA measurements provided evidence supporting the presence of oxygen-containing functional groups on the surface of exfoliated graphene, indicating that exfoliated graphene has similarities with graphene oxide. To investigate the interaction between the studied molecule and graphene flakes, we performed calculations on both pristine graphene and graphene containing epoxy group. Recent studies [53–57] have highlighted the critical role of defects and oxygen-containing groups on graphene oxide surfaces in facilitating molecular adsorption and favoring the functionalization process. To simplify our discussion, we will refer to the graphene pristine flake as G and the system representing graphene oxide as GO. Furthermore, we will use the abbreviations G-DMAD and GO-DMAD to denote the interaction between the molecule and pristine and oxidized substrates, respectively.

The DMAD molecule was placed in either the para or ortho configurations of the aromatic ring of graphene sheets to examine its attachment to both graphene-based systems (see Fig. 7). Our DFT results demonstrate that the adsorption of the molecule onto pristine graphene is not spontaneous since the ΔE is positive, requiring an energy of approximately 1 eV for the reaction to occur, resulting in a calculated ΔE value of 0.96 eV/molecule (1.54 eV/molecule) in the ortho (para) configuration. However, when considering the adsorption of DMAD on the defective aromatic ring of the epoxide, the ΔE values become negative, indicating that the adsorption process becomes exothermic in the presence of defects. Specifically, the most favourable configuration shows DMAD chemisorbed in the para configuration with a ΔE of −0.26 eV/molecule, as illustrated in Fig. 7. In the final and most stable configuration, the ester groups, which were originally conjugated with a C—C triple bond, are now bonded to two C atoms with a bond length equal to 1.35 Å, typical of a double bond. Additionally, the latter ones form two covalent bonds with the graphene matrix atoms, with a length of 1.56 Å.

Then we calculated the absorption spectrum of the molecule adsorbed on the graphene, (both pristine and oxidized) flake within the TDDFT approach and compared it with the absorption spectrum of the molecule before being attached to graphene. In this case, the graphene sheet was represented by a cluster containing seven benzene rings (see section S.4 of the supporting information), since it has been shown that such model cluster is suitable for obtaining accurate electronic and optical properties while keeping computational costs low [58,59].

The calculated absorption spectra are reported in Fig. 7c. It is apparent that when DMAD is chemically bound to graphene an absorption peak appears at low frequency (between 500 and 600 nm). These findings are consistent with the fluorescence signal observed for the functionalized graphene and reported in Fig. 3. Our TDDFT simulations further indicate that the origin of this peak can be attributed to the hybridization between the π orbitals of DMAD and those of the graphene matrix. This conclusion is supported by the response charge calculation for the first main absorption peak at 2.2 eV, which was

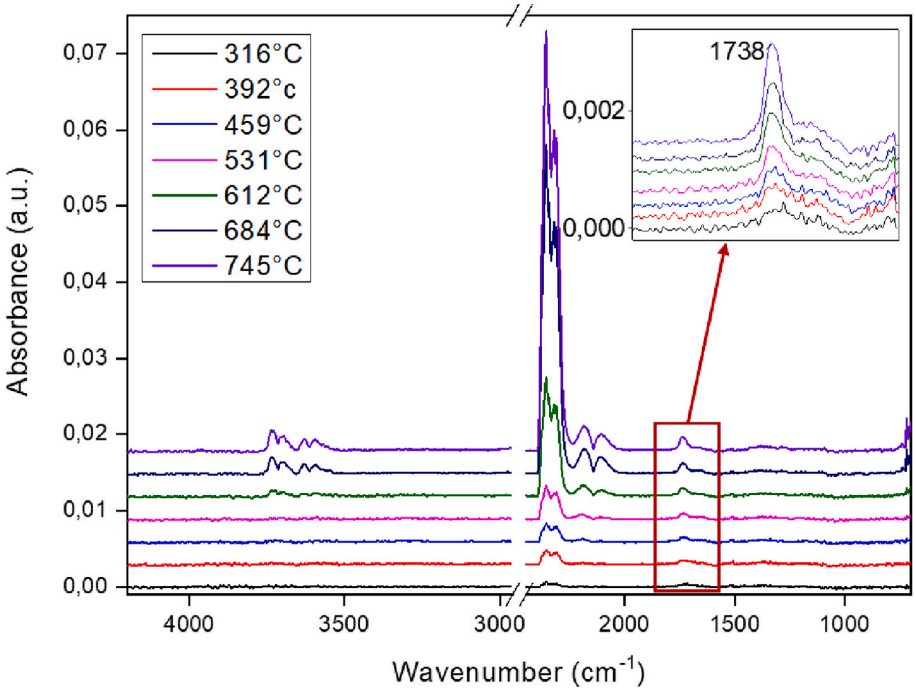

Fig. 5. Gas phase IR of M60 at different temperature.

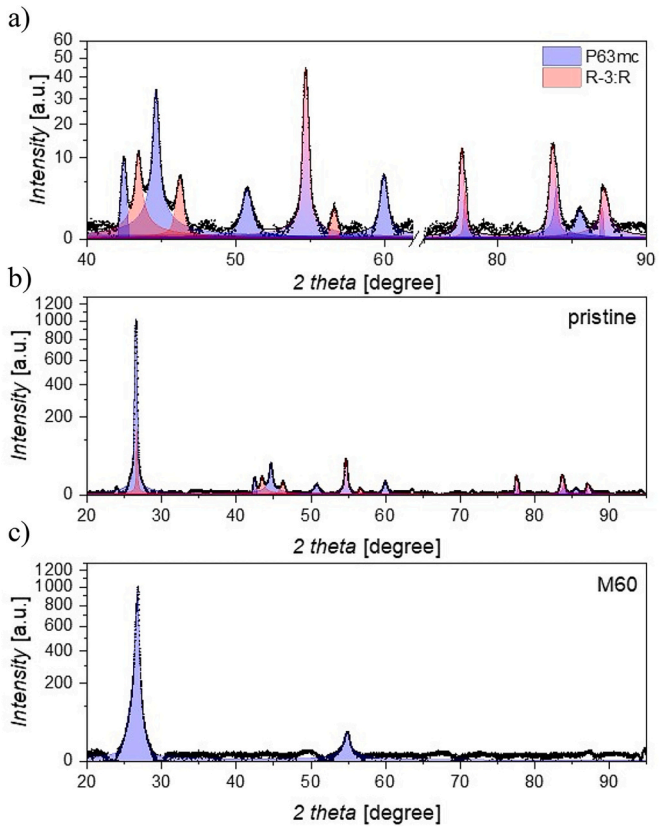

Fig. 6. Pattern of the pristine powder with an (a) enlargement of the regions of 40–62° and 75–90 degrees and (b) the whole pattern. (c) Pattern of the sample M60. Both the patterns have been subtracted with the background radiation and for (a) and (b) the broad peak of GO was subtracted.

performed for an electric field polarized along the longitudinal axis of the DMAD molecule (Fig. 8).

The theoretical analysis highlights the pivotal role that extrinsic defects within the graphene matrix play in such a functionalization mechanism and offer valuable insights into the electronic and optical properties of the adsorbed DMAD molecule, and further our understanding of its interaction with the graphene matrix.

3.7. Electrochemical analyses

The evaluation of the M60 performances started by evaluating the *i-v* characteristics by means of CV analysis at 0.2 mV s^{-1}. The results of the CV measurements are shown in Fig. 9. In Fig. 9a, the evolution of 20 voltammetric cycles is reported. During the first cathodic sweep, the M60 electrode is brought from its open circuit potential down to 0.1 V vs Li/Li^{+}. During this first reduction path, it is evident the formation of the SEI layer as suggested by the intense reduction currents. Further, the first cycle irreversible capacity loss is non negligible as evident form the first anodic sweep. By analysing the initial reduction and oxidation charges, the initial coulombic efficiency is about 8.4 %, meaning that most of the energy is consumed in favour to the SEI formation. The low specific current is due to the reduced potential window because only the 1st intercalation stage is completely taken in the calculation. Indeed, further scans in the full potential window revealed the complete intercalation and de-intercalation stages as reported in Fig. 9bc [60]. It can be noticed that the electrode keeps good electrochemical reversibility, and the discharge capacity increases from 56.3 mA g^{-1} at the reduced potential window up to 162.3 mAh g^{-1} in the wider one. Further, the electrode stabilizes in few cycles as it can be better appreciated by the CV reported in Fig. 9b in an extended potential window. Upon interface stabilization, the electrode reaches 95 % coulombic efficiency. Remarkably, the intercalation and de-intercalation peaks shift towards the same potential, akin to a more electrochemically reversible system. Indeed, as reported and evidenced in Fig. 9b, the potential difference between the first intercalation and the de-intercalation peaks is approximatively 50 mV, close to the value of a one-electron process.

The open circuit potential impedance of the modified graphitic electrode is shown in Fig. S31. The measurement shows a semicircle in the high frequency range that can be associated with a possible percolation path of the charges among the flakes, due to the binder. Overall, at the open circuit potential, prior to Li intercalation, the electrode is showing the expected blocking behaviour and a series resistance of 4 Ω.

After the CV analysis the M60 was subject to GCD at different current rates set as C-rates. The rates were {1/10, 1/5, 1/2, 1, 2, 5, 10} C. It is worth noticing that the present C-rate values correspond to {37, 75, 185, 370, 745, 1860, 3720} mA g^{-1}. In Fig. 9c are reported the results of the galvanostatic cycling test. It shows the potential profile at the C-rate of C/10 (~40 mA g^{-1}). The three stages are clearly visible. The first one occurs at about 80 mV at constant plateau, the second one approximatively around 123 mV while the last one occurs around 200 mV. This result goes in good agreement with the oxidation branch of the CV scan of Fig. 9b. In Fig. 9d it is shown the result concerning the rate capability test. The M60 electrode retains the initial discharge capacity rated at 176 mAh g-1 at the C-rate of C/5 (~75 mA g^{-1}). Remarkably, the electrode retains 57 % of its initial capacity at the C-rate of 10C (~4.0 A g^{-1}), which is an interesting result considering the standard rate capabilities of Supercapacitor electrodes. This relatively high-power capability can be attributed to the defective state of M60 suggested by the Raman spectrum [61]. According to the results of Lucchese et al., the average inter-defect distance is 13.51 nm, which is a quite compatible result with respect to the crystallite size provided by XRD [62]. As suggested by the XRD analysis, the layer spacing is reduced from ~3.35 Å to 3.34 Å, increasing the material density which is positive in terms of volumetric energy density.

The Ragone plot concerning the energy and power capabilities of the investigated electrode material was derived from the C-Rate analysis and reported in Fig. S30. The material was tested in a power density range from 10 W kg^{-1} up to 1 kW kg^{-1}. Remarkably, the specific energy ranges from 50 Wh kg^{-1} to approximatively 20 Wh kg^{-1}.

The presented results are in line with literature reports [63,64] The reduced specific capacity can be addressed to a large crystallite owing to a bigger diffusion path, although the material defectiveness [65]. These results represent a promising achievement. One of the cheapest, environmentally friendly, and convenient high-power and high-density system is represented by activated carbon-based Li-ion capacitors (LIC). These materials feature specific capacities of less than 15mAh g^{-1} in half-cell configuration. This specific capacity value is compliant with the last intercalation stage capacity at a lower potential, which is also a recommended operative point for LIC. Hence it is sufficient to develop high-rate capability graphite materials without the need to scarify a huge amount of energy to pre-lithiate graphite to desired levels, to meet a good balance during the charge balancing procedures aimed to maximize the final device performance.

4. Conclusions

The reactivity of graphene with DMAD was investigated using a microwave-assisted DA reaction, and the physical, chemical, and electrochemical properties of the resulting products were thoroughly analyzed. The functionalization mechanism and the role of defects introduced during the exfoliation process were examined. The interaction between the DMAD molecule and both pristine and oxidized graphene flakes was delved into, with DFT calculations revealing that the adsorption of the DMAD molecule onto pristine graphene required the presence of defects on the epoxide to become exothermic. These findings emphasized the crucial role of extrinsic defects within the graphene

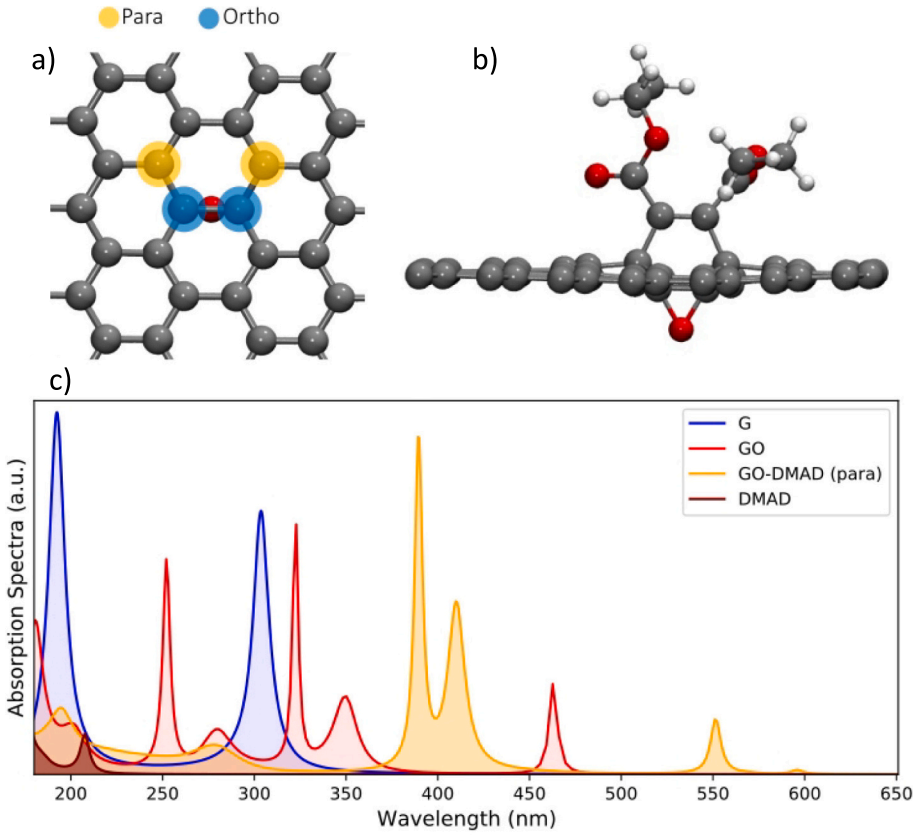

Fig. 7. Ball-and-stick representation of graphene oxide and the absorption of MDAD molecule onto graphene oxide (top panels). C atoms are represented in grey, O in red, H in white. The yellow and blue-highlighted C atoms correspond to the anchor site of the molecule in the para and ortho configurations, respectively. The TDDFT absorption spectra of the isolated MDAD, G, GO and GO-MDAD in para configuration (bottom panel). (For interpretation of the references to colour in this figure legend, the reader is referred to the web version of this article.)

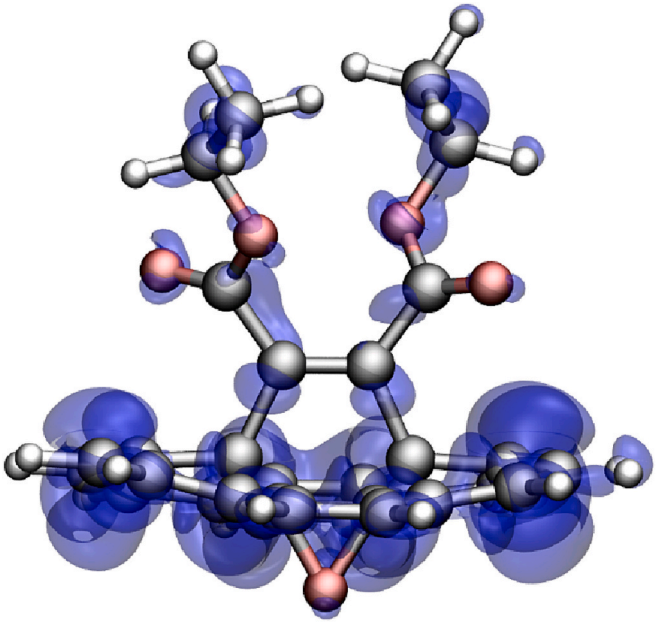

Fig. 8. Response charge of DMAD-GO molecular system in para configuration, for the first main absorption peak at 2.2 eV. The perturbation is oriented along the long axis of the DMAD molecule.

matrix in the functionalization process and provided valuable insights into the electronic and optical properties of the adsorbed DMAD molecule. These insights could contribute to the advancement of more efficient and cost-effective methods for large-scale production of high-quality graphene-based materials.

Carbon-based materials typically offer lower energy density compared to lithium-ion battery electrodes. Enhancing the energy storage capacity of carbon-based electrodes is a critical challenge in Li-ion capacitor development. Researchers are exploring strategies to increase the specific surface area and optimize the pore structure of carbon materials to improve their energy storage capabilities. Concerning the power density, while carbon materials exhibit high power capability, achieving even higher power density is desirable for Li-ion capacitors. The challenge lies in enhancing the kinetics of charge transfer and ion diffusion within the electrode material. Developing carbon-based materials with improved conductivity and designing electrode architectures that facilitate efficient ion transport are areas of active research. Moreover Li-ion capacitors should maintain stable performance over numerous charge-discharge cycles. Carbon-based electrodes are susceptible to structural degradation and the formation of solid-electrolyte interphase (SEI) layers during cycling, which can impair performance. Researchers are focused on developing carbon materials with enhanced structural stability and designing electrode formulations that mitigate the formation of SEI layers, ensuring prolonged cycling stability. Finally, Li-ion capacitors should exhibit excellent performance at high charge-discharge rates. However, carbon-based electrodes can experience limitations in terms of ion diffusion and charge transfer kinetics, leading to reduced rate capability. Overcoming these limitations involves

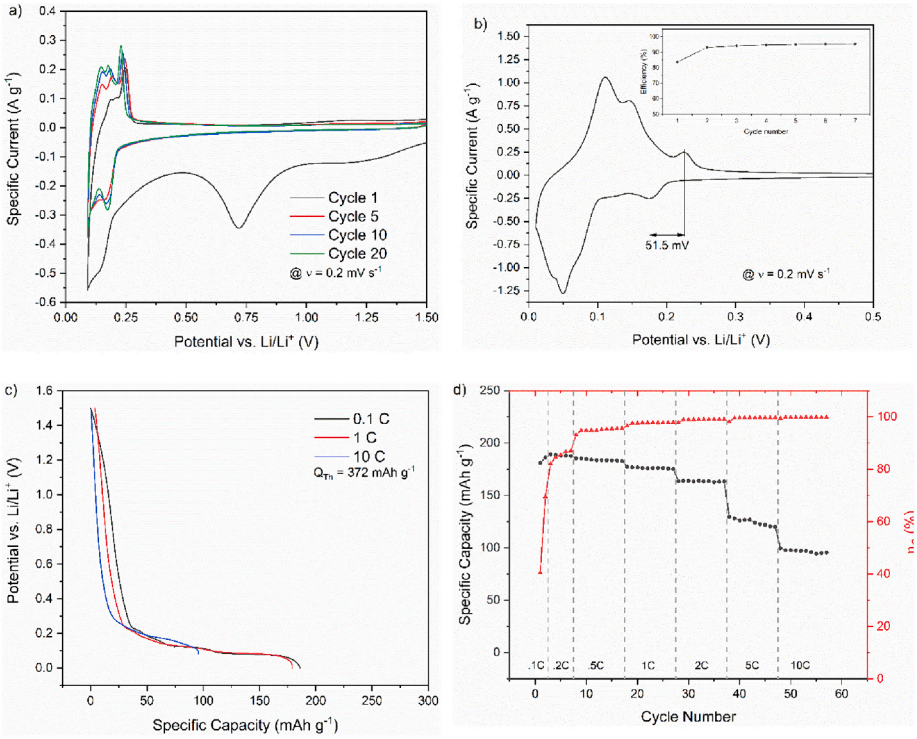

Fig. 9. Cyclic voltammetry analysis of the M60 sample exploited as anode material. In a) the evolution of 20 CV cycles carried out at 0.2 mV s^{-1} showing an important first cycle initial capacity loss due to the SEI formation. In the inset of a) it is shown that the material stabilizes towards a more electrochemically reversible state. In b) a highlight of cycle 20 showing that the potential difference between the two peaks due to the first intercalation stage (reduction) is c.a. 60 mV apart from the last de-intercalation potential (oxidation) akin to a reversible process.

designing carbon materials with improved ion transport properties and optimizing electrode structures to facilitate faster charge-discharge processes.

Here instead electrochemical analyses of the M60 anode material for Li-ion energy storage devices demonstrated its excellent electrochemical reversibility and rate capability. Material stabilization was observed after a few cycles, resulting in a coulombic efficiency of up to 95 % and a discharge capacity of 162.3 mA h g^{-1}. The galvanostatic cycling test indicated that the M60 electrode retained 57 % of its initial capacity at a C-rate of 10C, indicating its high-power capability. These promising results suggest that M60 could be a potential material for Li-ion capacitors, offering a specific capacity that aligns with the last intercalation stage capacity at a lower potential.

CRediT authorship contribution statement

Silvia Mazzotta: Writing – review & editing, Writing – original draft, Validation, Methodology, Investigation, Formal analysis, Data curation, Conceptualization. **Alberto Martis:** Methodology, Investigation. **Mara Serrapede:** Writing – review & editing, Writing – original draft, Methodology, Formal analysis, Data curation. **Pietro Zaccagnini:** Writing – review & editing, Writing – original draft, Methodology, Formal analysis, Data curation. **Stefano Bianco:** Writing – review & editing, Investigation, Data curation. **Giancarlo Cicero:** Conceptualization, Data curation, Methodology, Writing – review & editing. **Francesca Verga:** Project administration, Supervision, Writing – review & editing. **Fabrizio Pirri:** Funding acquisition, Resources, Supervision, Writing – review & editing. **Andrea Lamberti:** Resources, Writing – original draft, Writing – review & editing. **Sergio Bocchini:** Conceptualization, Data curation, Formal analysis, Investigation, Methodology, Resources, Supervision, Validation, Writing – original draft, Writing – review & editing.

Declaration of competing interest

The authors declare that they have no known competing financial interests or personal relationships that could have appeared to influence the work reported in this paper.

Data availability

No data was used for the research described in the article.

Acknowledgements

This paper and related research have been conducted during and with the support of the Italian national inter-university PhD course in Sustainable Development and Climate change (link: www.phd-sdc.it).

Authors wish to thank European Union for the financial support through the Next Generation EU- projects “Nord Ovest Digitale E Sostenibile-NODES” (PNRR, D.D. n.1054 June 23, 2022), NEST “Network for Energy Sustainable Transition- NEST”(PE0000021, D.D. n.341 March 15, 2022), PNRR Mission 4 “Education and Research”—Component 2 “From research to business”—Investment 3.1 “Fund for the realization of an integrated system of research and innovation infrastructures”—Call for tender No. n. 3264 of 28/12/2021 of Italian Ministry of Research funded by the European Union—NextGenerationEU—Project code: IR0000027, Concession Decree No. 128 of 21/06/2022 adopted by the Italian Ministry of Research, CUP: B33C22000710006, Project title: iENTRANCE. Authors also acknowledge Ministero dello Sviluppo Economico (MISE) and Ministero della Transizione Ecologica (MITE) for the financial support. This manuscript reflects only the authors' views and opinions, neither the European Union nor the European Commission can be considered responsible for them.

Declaration of generative AI in scientific writing

During the preparation of this work the authors used ChatGPT to avoid grammar mistakes. After using this service, the authors reviewed and edited the content as needed and take full responsibility for the content of the publication.

Appendix A. Supplementary data

Supplementary data to this article can be found online at https://doi.org/10.1016/j.est.2024.111857.

References

[1] V. Georgakilas, M. Otyepka, A.B. Bourlinos, V. Chandra, N. Kim, K.C. Kemp, P. Hobza, R. Zboril, K.S. Kim, Functionalization of Graphene: Covalent and Non-Covalent Approaches, Derivatives and Applications, Adv. Mater. 18 (2020) 2001086.

[2] J.-W. Lee, M. Kim, W. Na, S. Man Hong, C.M. Koo, Fabrication of high quality graphene nanosheets via a spontaneous electrochemical reaction process, Carbon 91 (2015) 527–534.

[3] A. Dato, V. Radmilovic, Z. Lee, J. Phillips, M. Frenklach, Substrate-Free Gas-Phase Synthesis of Graphene Sheets, Nano Lett. 8 (7) (2008) 2012–2016.

[4] X. Zhang, A.C. Coleman, N. Katsonis, W.R. Browne, B.J. van Wees, B.L. Feringa, Dispersion of graphene in ethanol using a simple solvent exchange method, Chem. Commun. 46 (2010) 7539–7541.

[5] Z. Li, J. Dong, L. Wang, Y. Zhang, T. Zhuang, H. Wang, X. Cui, Z., Wang A power-triggered preparation strategy of nanostructured inorganics: sonosynthesis, Nanoscale Adv. 3 (2021) 2423–2447.

[6] H. Xu, B.W. Zeigera, K.S. Suslick, Sonochemical synthesis of nanomaterials, Chem. Soc. Rev. 42 (7) (2013) 2555–2567.

[7] Z. Li, J. Dong, A.H. Zhang, Y. Zhang, H. Wang, X. Cui, Z. Wang, Sonochemical catalysis as a unique strategy for thefabrication of nano−/micro-structured inorganics, Nanoscale Adv. 3 (2021) 41–72.

[8] S. Sarkar, E. Bekyarova, R.C. Haddon, Chemistry at the Dirac Point: DielsAlderReactivity of Graphene, Acc. Chem. Res. 45 (4) (2012) 673–682.

[9] J. Zhang, K. Hu, Q. Ouyang, Q. Gui, X. Chen, One-step functionalization of graphene via Diels–Alderreaction for improvement of dispersibility, Front. Mater. Sci. 14 (2) (2020) 198–210.

[10] A. Ferretti, S. Sinha, L. Sagresti, E. Araya-Hermosilla, M. Prato, V. Mattoli, A. Pucci, G. Brancato, One-step functionalization of mildly and strongly reduced graphene oxide with maleimide: an experimental and theoretical investigation of the Diels–Alder [4+2] cycloaddition reaction, Phys. Chem. Chem. Phys. 24 (2022) 2491–2503.

[11] P.A. Denis, Organic Chemistry of Graphene: The Diels–Alder Reaction, Chem. Eur. J. 19 (2013) 15719–15725.

[12] Z. Feng, H. Zuo, J. Hu, B. Yu, N. Ning, M. Tian, L. Zhang, In Situ Exfoliation of Graphite into Graphene Nanosheets in Elastomer Composites Based on Diels−Alder Reaction during Melt Blending, Ind. Eng. Chem. Res. 58 (2019) 13182–13189.

[13] J. Zhang, Q. Ouyang, Q. Gui, X. Chen, Ultrasonic-Assisted Diels–Alder Reaction Exfoliation of Graphite into Graphene with High ResveratrolAdsorption Capacity, Nanomaterials 11 (2021) 3060.

[14] N.F. Torkaman, M. Kley, W. Bremser, R. Wilhelm, Reversible functionalization and exfoliation of graphite by a Diels–Alder reaction with furfurylamine, RSC Adv. 12 (2022) 17249–17256.

[15] J. Asenbauer, T. Eisenmann, M. Kuenzel, A. Kazzazi, Z. Chen, D. Bresser, The success story of graphite as a lithium-ion anode material – fundamentals, remaining challenges, and recent developments including silicon (oxide) composites, Sustain. Energy Fuels 4 (2020) 5387–5416.

[16] B. Babu, P. Simon, A. Balducci, Fast Charging Materials for High Power Applications, Adv. Energy Mater. 10 (29) (2020) 2001128.

[17] K. Kinoshita, K. Zaghib, Negative Electrodes for Li-Ion Batteries, J. Power Sources 110 (2002) 416–423.

[18] L. Zou, F. Kang, Y.-P. Zheng, W. Shen, Modified natural flake graphite with high cycle performance as anode material in lithium ion batteries, Electrochim. Acta 54 (15) (2009) 3930–3934.

[19] V. Cauda, D. Pugliese, N. Garino, A. Sacco, S. Bianco, F. Bella, A. Lamberti, C. Gerbaldi, Multi-functional energy conversion and storage electrodes using flower-like Zinc oxide nanostructures, Energy 65 (2014) 639–646.

[20] A. Lamberti, M. Destro, S. Bianco, M. Quaglio, A. Chiodoni, C.F. Pirri, C. Gerbaldi, Facile fabrication of cuprous oxide nanocomposite anode films for flexible Li-ion batteries via thermal oxidation, Electrochim. Acta 86 (2012) 323–329.

[21] A. Lamberti, N. Garino, A. Sacco, S. Bianco, D. Manfredi, C. Gerbaldi, Vertically aligned TiO2 nanotube array for high rate Li-based micro-battery anodes with improved durability, Electrochim. Acta 102 (2013) 233–239.

[22] A. Lamberti, N. Garino, A. Sacco, S. Bianco, A. Chiodoni, C. Gerbaldi, As-grown vertically aligned amorphous TiO2 nanotube arrays as high-rate Li-based micro-battery anodes with improved long-term performance, Electrochim. Acta 151 (2015) 222–229.

[23] A. de la Hoz, A. Díaz-Ortiz, P. Prieto, in: G. Stefanidis, A. Stankiewicz (Eds.), Alternative Energy Sources for Green Chemistry, The Royal Society of Chemistry, 2016, pp. 1–33.

[24] C.O. Kappe, A. Stadler, Microwaves in Organic and Medicinal Chemistry. 2nd, Wiley, 2012.

[25] R. Sanghi, V. Singh, Green Chemistry for Environmental Remediation, Wiley, 2012, pp. 379–424.

[26] I. Milosevic, E. Guenin, Y. Lalatonne, F. Benyettou, C. de Montferrand, F. Geinguenaud, L. Motte, N.N. Opembe, H. Huang, S.L. Suib, D.V. Szabó, in: H. Satoshi, N. Serpone (Eds.), Microwaves in Nanoparticle Synthesis: Fundamentals and Applications, Wiley, 2013, pp. 75–143.

[27] N.E. Leadbeater, in: P. Knochel, G.A. Molander (Eds.), Comprehensive Organic Synthesis: Second Edition 19, Elsevier Ltd, 2014, pp. 234–286.

[28] R.B. Nasir Baig, R.S. Varma, Alternative energy input: Mechanochemical, microwave and ultrasound-assisted organic synthesis, Chem. Soc. Rev. 41 (4) (2012) 1559–1584.

[29] A. de la Hoz, A. Díaz-Ortiz, A. Moreno, Microwaves in organic synthesis. Thermal and non-thermal microwave effects, Chem. Soc. Rev. 34 (2) (2005) 164–178.

[30] J.N. Coleman, Liquid exfoliation of defect-free graphene, Acc. Chem. Res. 46 (2013) 14–22.

[31] Y. Hernandez, V. Nicolosi, M. Lotya, F.M. Blighe, Z. Sun, S. De, I.T. McGovern, B. Holland, M. Byrne, Y.K. Gun'Ko, J.J. Boland, P. Niraj, G. Duesberg, S. Krishnamurthy, R. Goodhue, J. Hutchison, V. Scardaci, A.C. Ferrari, J. N. Coleman, High-yield production of graphene by liquid-phase exfoliation of graphite, Nat. Nanotechnol. 3 (9) (2008) 563–568.

[32] A. Martis, M. Fontana, M. Serrapede, S. Bianco, A. Chiodoni, C.F. Pirri, S. Bocchini, Production of Graphene Stably Dispersible in Ethanol by Microwave Reaction, Colloids and Interfaces 6 (2022) 4.

[33] F. Tuinstra, J.L. Koenig, Raman spectrum of graphite, J. Chem. Phys. 53 (3) (1970) 1126–1130.

[34] T.L. Slager, F.M. Prozonic, Simple methods for calibrating IR in TGA/IR analyses, Thermochim. Acta 426 (1–2) (2005) 93–99.

[35] G. Surekha, FTIR, Raman and XRD analysis of graphene oxide films prepared by modified Hummers method, J. Phys. Conf. Ser. 1945 (2020) 012012.

[36] Beer–Lambert law. IUPAC Compendium of Chemical Terminology, 3rd ed. International Union of Pure and Applied Chemistry, 2006. Online version 3.0.1, 2019.

[37] J. Shang, L. Ma, J. Li, et al., The Origin of Fluorescence from Graphene Oxide, Sci. Rep. 2 (2012) 792.

[38] P. Zheng, N. Wu, Fluorescence and Sensing Applications of Graphene Oxide and Graphene Quantum Dots: A Review, Chem. Asian J. 12 (2017) 2343–2353.

[39] F. La Mantia, P. Novak, Online Detection of Reductive CO2 Development at Graphite Electrodes in the 1 M LiPF6, EC:DMC Battery Electrolyte, Electrochem. Solid-State Lett. 11 (5) (2008) A84.

[40] P. Giannozzi, et al., QUANTUM ESPRESSO: a modular and open-source software project for quantum simulations of materials, J. Phys. Condens. Matter 21 (39) (2009) 395502.

[41] P. Giannozzi, et al., Advanced capabilities for materials modelling with Quantum ESPRESSO, J. Phys. Condens. Matter 29 (2017) 46.

[42] J.P. Perdew, K. Burke, M. Ernzerhof, Generalized Gradient Approximation Made Simple, 1996.

[43] A.M. Rappe, K.M. Rabe, E. Kaxiras, J.D. Joannopoulos, Optimized pseudopotentials, 1990, p. 15.

[44] S. Grimme, Semiempirical GGA-Type Density Functional Constructed with a Long-Range Dispersion Correction, J. Comput. Chem. 27 (2006) 1787–1799.

[45] H.J. Monkhorst, J.D. Pack, Special points for Brillonin-zone integrations, 1976.

[46] G. Henkelman, B.P. Uberuaga, H. Jónsson, Climbing-Image NEB Method for Finding Saddle Points and Minimum Energy Paths, J. Chem. Phys. 113 (2000) 9901.

[47] O.B. Malcıoğlu, R. Gebauer, D. Rocca, S. Baroni, TurboTDDFT - A code for the simulation of molecular spectra using the Liouville-Lanczos approach to time-dependent density-functional perturbation theory, Comput. Phys. Commun. 182 (8) (2011) 1744–1754.

[48] J. Heyd, G.E. Scuseria, M. Ernzerhof, Hybrid functionals based on a screened Coulomb potential, J. Chem. Phys. 118 (2003).

[49] J. Heyd, G.E. Scuseria, M. Ernzerhof, Erratum: Hybrid functionals based on a screened Coulomb potential, J. Chem. Phys. 124 (2006) 21.

[50] A.C. Ferrari, J.C. Meyer, V. Scardaci, C. Casiraghi, M. Lazzeri, F. Mauri, S. Piscanec, D. Jiang, K.S. Novoselov, S. Roth, A.K. Geim, Raman Spectrum of Graphene and Graphene Layers, Phys. Rev. Lett. 97 (2006) 1–4.

[51] L.M. Malard, M.A. Pimenta, G. Dresselhaus, M.S. Dresselhaus, Raman spectroscopy in graphene, Phys. Rep. 473 (2009) 51–87.

[52] K. Kinoshita, Carbon in electrochemical and physicochemical properties, Wiley, 1988, p. 533.

[53] C.K. Chuaa, M. Pumera, Covalent chemistry on graphene, Chem. Soc. Rev. 42 (2013) 3222–3233.

[54] M. Rajapakse, et al., Intercalation as a versatile tool for fabrication, property tuning, and phase transitions in 2D materials, npj 2D Materials and Applications 5 (2021) 1–21.

[55] Y. Cao, Z. Lai, J. Feng, P. Wu, Graphene oxide sheets covalently functionalized with block copolymers*via* click chemistry as reinforcing fillers, J. Mater. Chem. 21 (2011) 9271–9278.

[56] H.K. Choi, et al., Influences of carboxyl functionalization of intercalators on exfoliation of graphite oxide: a molecular dynamics simulation, Phys. Chem. Chem. Phys. 20 (2018) 28616–28622.

[57] W. Yu, L. Sisi, Y. Haiyan, L. Jie, Progress in the functional modification of graphene/graphene oxide: a review, RSC Adv. 10 (2020) 15328–15345.

[58] N. Shahzad, F. Risplendi, D. Pugliese, S. Bianco, A. Sacco, A. Lamberti, R. Gazia, E. Tresso, G. Cicero, Comparison of Hemi-Squaraine Sensitized TiO2 and ZnO

Photoanodes for DSSC Applications, J. Phys. Chem. C 117 (44) (2013) 22778–22783.
[59] F. Risplendi, G. Cicero, Co-Adsorbent Effect on the Sensitization of TiO2 and ZnO Surfaces: A Theoretical Study, J. Phys. Chem. C 119 (49) (2015) 27348–27353.
[60] H. Zhang, Y. Yang, D. Ren, L. Wang, X. He, Graphite as anode materials: Fundamental mechanism, recent progress and advances, Energy Storage Mater. 2021 (36) (2021) 147–170.
[61] Z. Chen, Y. Liu, Y. Zhang, F. Shen, G. Yang, L. Wang, X. Zhang, Y. He, L. Luo, S. Deng, Ultrafine layered graphite as an anode material for lithium ion batteries, Mater. Lett. 229 (2018) 134–137.
[62] M.M. Lucchese, F. Stavale, E.H. Martins Ferreira, C. Vilani, M.V.O. Moutinho, Rodrigo B. Capaz, C.A. Achete, A. Jorio, Quantifying ion-induced defects and Raman relaxation length in graphene. Carbon 48, 2010, pp. 1592–1597.
[63] Q. Cheng and Y. Zhang. Multi-Channel Graphite for High-Rate Lithium Ion Battery. Journal of The Electrochemical Society, 165, 5, A1104.
[64] H. Buqa, D. Goers, M. Holzapfel, M.E. Spahr, P. Novák, High Rate Capability of Graphite Negative Electrodes for Lithium-Ion Batteries, J. Electrochem. Soc. 152 (2) (2005) A474.
[65] J. Inamoto, Y. Matsuo, M. Katsumi, S. Uchida, M. Ishikawa, T. Masuyama, K. Tsukamoto, Y. Sato, Effect of hydrogen-gas treatment on the local structure of graphene-like graphite, Carbon 163 (2020) 162–168.